Research Article

ADVANCED PHOTONICS

First demonstration of lithium niobate photonic chip for dense wavelength-division multiplexing transmitters

Hongxuan Liu,[a,†] Bingcheng Pan,[a,†] Huan Li,[a] Zejie Yu,[a,b,c] Liu Liu,[a,b,c,d] Yaocheng Shi,[a,b,c,d] and Daoxin Dai[a,b,c,d,*]

[a]Zhejiang University, State Key Laboratory for Extreme Photonics and Instrumentation, College of Optical Science and Engineering, International Research Center for Advanced Photonics, Hangzhou, China
[b]Jiaxing Key Laboratory of Photonic Sensing and Intelligent Imaging, Jiaxing, China
[c]Jiaxing Research Institute Zhejiang University, Intelligent Optics and Photonics Research Center, Jiaxing, China
[d]Zhejiang University, Ningbo Research Institute, Ningbo, China

Abstract. Modern optical communications rely heavily on dense wavelength-division multiplexing (DWDM) technology because of its capability of significantly increasing transmission channels. Here, we demonstrate, for the first time to the best of our knowledge, a compact photonic chip for DWDM transmitters on lithium-niobate-on-insulator (LNOI) by introducing the array of 2×2 Fabry–Perot (FP) cavity electro-optic (EO) modulators. A four-channel LNOI photonic chip for DWDM is designed and realized with a channel spacing of 1.6 nm (which is the narrowest one reported until now for LNOI optical transmitters), exhibiting a total excess loss of 1.3 dB and high 3-dB EO bandwidths of >67 GHz for all channels. Specifically, these four 2×2 FP cavities are designed with broadened LNOI photonic waveguides in the cavity sections, and they are placed very closely on the chip so that their resonance wavelengths are aligned precisely with the desired channel-spacing of ~1.6 nm. Finally, the generation of 4×80-Gbps on–off keying and 4×100-Gbps PAM4 signals is demonstrated successfully with four channels, and the power consumption is as low as ~5.1 fJ/bit. The present photonic chip has a compact footprint of about 0.78 mm × 0.58 mm, showing great potential to work with more than four channels and to be very useful for future large-capacity optical links.

Keywords: lithium niobate; dense wavelength-division multiplexing; electro-optic modulator; transmitter; Fabry–Perot cavity.

Received Jun. 4, 2024; revised manuscript received Sep. 10, 2024; accepted for publication Sep. 25, 2024; published online Oct. 21, 2024.

[DOI: 10.1117/1.AP.6.6.066001]

1 Introduction

Ultrahigh-capacity data transmissions have been in high demand because of the increasing applications of data centers and 5G systems.[1–4] Particularly, wavelength-division multiplexing (WDM) has been developed successfully and utilized widely for enhancing the link capacity by multiplexing a number of optical channels with different wavelengths.[5,6] Accordingly, it is always very important to develop high-performance transmitters and receivers for WDM systems. As is well known, for the realization of optical transmitters, one usually desires to monolithically integrate the key elements, such as high-speed optical modulators and WDM filters.[7–9] Some silicon photonic chips have been developed for WDM transmitters by integrating modulators and WDM filters with the technology of silicon photonics,[10–12] which has been regarded as one of the most promising options for photonic integration because of the unique advantages of high integration density and complementary-metal-oxide-semiconductor (CMOS) compatibility. In recent years, silicon photonics WDM transmitters[8,10,13–17] have been improved on with modulation bandwidth, excess loss (EL), digital signal processing (DSP), and thermal controlling, featuring a total capacity up to 4×112 Gbps[14] and 32×18 Gbps[15] (see Table S1 in the Supplementary Material). However, silicon photonic modulators based on the plasma dispersion effect are

*Address all correspondence to Daoxin Dai, dxdai@zju.edu.cn
†These authors contributed equally to this work.

inherently limited in terms of linearity and insertion loss because of the nonideal underlying EO mechanism. Moreover, these modulators deliver a power consumption at the level of tens or even hundreds of fJ/bit in general and are highly dependent on thermal control, which underlies the concern for the total energy consumption when scaling transmitters further.

Recently, lithium niobate (LN) has been reactivated because lithium-niobate-on-insulator (LNOI) wafers have become available commercially, and the fabrication processes have become mature.[18,19] Compared to silicon, LN intrinsically possesses some unique material properties, including its attractive electro-optic (EO) effect.[20] Particularly, LNOI photonic waveguides have strong optical and electric field confinement, enabling efficient EO modulation.[21–23] Therefore, LNOI photonics is highly promising for new-generation integrated photonics.

In recent years, LNOI EO modulators have been developed successfully with high bandwidths, low driving voltages, low ELs, etc. For example, LNOI Mach–Zehnder modulators (MZMs) were realized with the operation at CMOS-compatible voltages, presenting high 3-dB bandwidths of 45, 80, and 100 GHz, with a 20-, 10-, and 5-mm-long phase shifter, respectively.[24] Further improved MZMs with 10-mm-long capacitively loaded traveling-wave electrodes exhibit 3-dB bandwidths far exceeding 100 GHz, either on quartz substrates[25] or on undercut-etching silicon substrates.[26] To minimize the footprint, LNOI modulators based on microresonators have been extensively studied.[27–29] Among them, we have proposed a novel 2×2 FP cavity modulator, featuring an ultracompact footprint, low power consumption of 4.5 fJ/bit, and a wide 3-dB bandwidth of over 110 GHz.[30] Another promising structure of a microring consisting of a Mach–Zehnder interferometer with a coupling modulation breaks the photon lifetime limit and has presented an ultrahigh bandwidth of terahertz level in principle.[31] More recently, LNOI photonic chips for WDM transmitters have also been developed by integrating WDM filters and EO modulators. For example, an LNOI photonic chip for four-channel WDM transmitters has been demonstrated by combining four MZMs and a wavelength-division (de)multiplexer based on an angled multimode interferometer.[32] Alternatively, an LNOI chip has been realized by integrating four FP cavity modulators and four channels of photonic filters based on multimode waveguide gratings (MWGs).[33] Note that these reported LNOI photonic chips were developed with a channel spacing of as large as 20 nm, which does not satisfy the requirement of dense wavelength-division multiplexing (DWDM) systems yet.

One should note that the realization of DWDM filters is still very challenging when using x-cut LNOI photonic waveguides (which is desired for high-speed modulation). There are various structures available for realizing high-performance DWDM filters based on silicon photonic waveguides, such as arrayed waveguide gratings (AWGs),[34–36] microring resonators (MRRs),[37–39] as well as photonic crystal (PhC) cavities.[40] However, the situation for LNOI photonic waveguides is totally different because of the LN anisotropy and the sidewall tilting of the ridge waveguide. For example, when designing x-cut LNOI-based AWGs, the LN anisotropy makes it very difficult to calculate the accumulated phase delay accurately, which is the basis for the structure design of arrayed waveguides. Furthermore, when using LNOI photonic waveguides, one usually has to choose a large bending radius to achieve low loss and low cross talk light propagation, and thus the designed LNOI AWGs usually have a millimeter-scale size. In this case, some notable phase errors might be introduced and prevent to achieve low interchannel cross talk. Currently, there have been some attempts to develop AWGs with a z-cut LNOI wafer, but they show poor performances with high ELs and interchannel cross talk.[41,42] More importantly, they are incompatible for monolithic integration with x-cut-LNOI EO modulators. Alternatively, when developing DWDM filters based on LNOI MRRs, the challenge is that the free spectral range (FSR) is too limited to cover sufficient channels because a large bending radius is demanded to avoid notable ELs and mode hybridization.[43,44] The reported MRR filters on an x-cut LNOI usually have an FSR as small as around 2 nm.[27,45] Structures based on a multimode PhC nanobeam cavity[46] or topological PhC[47] can work as add–drop filters and avoid the bending section. However, it is difficult for the nanobeam cavity based on LNOI photonic waveguides to realize a sufficiently narrow full width at half-maximum (FWHM) bandwidth demanded for DWDM applications. Therefore, there have been no high-performance x-cut LNOI-based AWGs, MRRs, or PhCs for DWDM systems with narrow channel spacings until now.

Fortunately, our proposed 2×2 FP-cavity structure has the benefits of an ultrashort cavity, a low EL, as well as an ultracompact footprint.[29,30] More importantly, the reflected light is output from another port and is separated from the input port, owing to the introduction of MWGs and mode (de)multiplexers. Such a 2×2 FP cavity can work very similarly to ultracompact add–drop filters based on MRRs, while no bending section is needed in the 2×2 FP cavity, which makes it extremely attractive for developing DWDM filters based on LNOI photonic waveguides. In addition, such a 2×2 FP cavity can also be used to realize wavelength-selective optical modulators by applying an external electric field to the section of the FP cavity, in such a way that a 2×2 FP modulator simultaneously serves as a DWDM filter as well as an EO modulator. Furthermore, more than one 2×2 FP modulator can be cascaded to satisfy the demands of DWDM transmitters by carefully choosing the cavity lengths to align the resonance wavelengths with the DWDM grids.

On the other hand, it is often very challenging to achieve excellent wavelength alignment for cascaded cavity-based optical modulators due to the random fabrication deviations of the waveguide core width and the etching depth.[48] The wavelength misalignment is usually nanometer level in experiments,[49,50] for which the thermal tuning is often introduced for those silicon MRR-based optical modulators in WDM systems; thus some additional power consumption is needed. For LNOI photonics, low-efficiency thermo-optic tuning is not a good choice due to high power consumption, while EO tuning is hard to achieve in the wavelength-tuning range in nanometer scale. Therefore, it is still very desirable to achieve multichannel optical cavity modulators with uniform dense channel spacing for DWDM transmitters.

In this paper, we propose a compact LNOI photonic chip for DWDM transmitters based on multichannel 2×2 FP cavity-based EO modulators. The present photonic chip features a compact footprint of only 0.78 mm $\times$ 0.58 mm and a low EL of about 1.3 dB. More importantly, it has four wavelength channels with a dense channel spacing of 1.6 nm (which is the narrowest one reported until now for LNOI optical transmitters). Specifically, these four 2×2 FP cavities are placed very closely

on the chip, and they are designed with broadened LNOI photonic waveguides in the cavity sections. In this way, their resonance wavelengths become insensitive to the core-width variation, and they are aligned precisely with the desired channel spacing of ∼1.6 nm. The measured small-signal EO responses show that the present FP cavity modulators have 3-dB bandwidths of >67 GHz, while the interchannel EO cross talk is less than −7 dB in the range of 0.01 to 67 GHz. Finally, high-speed data transmissions with high-quality eye diagrams are demonstrated with 4×80 Gbps on–off keying (OOK) signals and 4×100 Gbps four-level pulse amplitude modulation (PAM4) signals, enabling high data transmission rate up to 400 Gbps in total. Compared to those DWDM transmitters reported previously with the data rate of 100 Gbps/channel (see Table S1 in the Supplementary Material), the LNOI photonic chip in this work shows a low EL, a larger EO bandwidth, and the power consumption is two to three orders lower. To our best knowledge, it is the first demonstration of LNOI photonic chip for DWDM transmitters with a channel spacing no more than 1.6 nm, providing a promising approach for high-capacity optical interconnects.

2 Structure and Design

Figure 1(a) shows the three-dimensional (3D) schematic configuration of the proposed LNOI photonic chip for DWDM transmitters. Here, multiple FP cavity EO modulators along the y-axis of the LN are resonant at different wavelengths and are cascaded at reflected ports through 180 deg waveguide bends, so that these FP cavities are arranged in parallel and thus the lateral separations between them are minimized. Metal electrodes are placed on both sides of these FP cavities for applying electric signals, and the ground electrodes are shared by the two adjacent FP cavities. Light composed of multiple wavelengths is coupled into and out of the chip through grating couplers.

More details of the FP cavity modulator structure are shown in Fig. 1(b). It can be seen that each FP cavity consists of a pair of MWGs with a short straight section in between and a mode (de)multiplexer. Here, the transverse-electric (TE) polarization mode is considered and light propagates along the y axis of the LN, so that the EO modulation efficiency can be maximized. The inset in Fig. 1(b) shows the cross section of the used LNOI ridge waveguide, whose sidewalls are tilted with the angle of

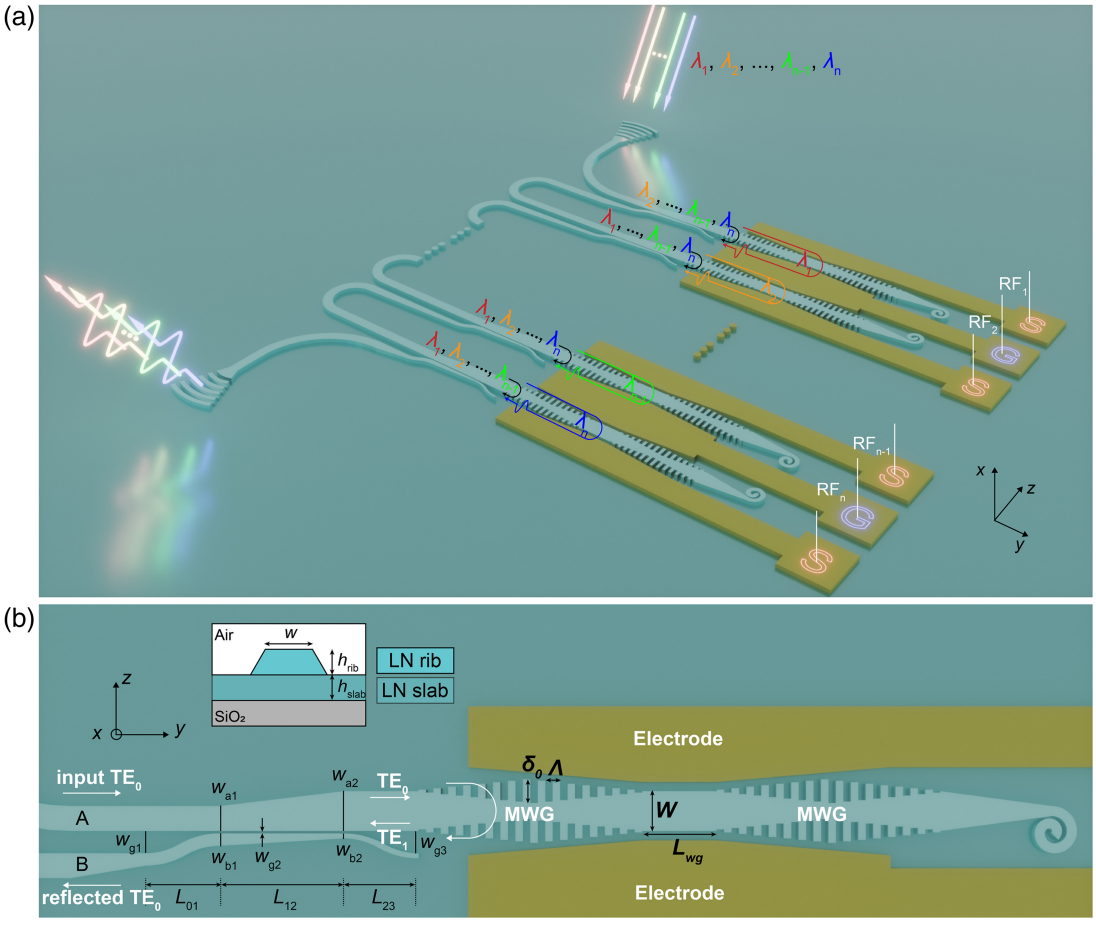

Fig. 1 (a) 3D schematic configuration of the proposed LNOI photonic chip for DWDM transmitters. N FP cavities with the same MWGs and mode MUXs but in different cavity lengths are cascaded through waveguide bends at the reflected port. (b) Top view of the FP cavity modulator unit, consists of a pair of MWGs with a short straight section in between and a mode (de)multiplexer (inset: cross section of the LNOI ridge waveguide).

30 deg (relative to the vertical axis). In this paper, the devices are based on an x-cut LNOI wafer with 400-nm-thick LN membrane, and the LN ridge waveguides have an etching depth of about 200 nm as well as an air upper cladding. The MWGs are designed to efficiently reflect the forward TE_0 (TE_1) mode into the backward TE_1 (TE_0) mode when operating in the Bragg wavelength band. In this way, when operating at the nonresonant wavelengths of the FP cavity, the TE_0 mode launched from the input side is reflected and converted to the TE_1 mode backward and then converted to the TE_0 mode at the reflected port by the mode (de)multiplexer. As a result, the reflected light is separated from the input light. Meanwhile, one has the forward TE_0 mode at the transmission side when operating around the resonance wavelengths of the FP cavity. Here, the through ports are terminated with sharp spiral waveguides, as shown in Fig. 1(b).

All cascaded FP cavities have the same structural parameters for the MWGs and mode (de)multiplexers, except for the length of the straight section between the MWGs. Hence, the cavity length varies, resulting in a change in the resonance wavelength. As shown in Fig. 1(a), all optical carriers with the wavelengths $\lambda_1, \lambda_2, \ldots, \lambda_n$ are input together from the input port. Each wavelength λ_i $(i = 1, 2, \ldots, n)$ is placed near the resonance wavelength of the FP cavity corresponding to channel #i. When light enters the FP cavity of channel #1, the wavelength channel of λ_1 resonates in the FP cavity, while the other wavelength-channels of $\lambda_2, \ldots, \lambda_n$ are reflected with high efficiency. By applying electrical signals to the ground/signal electrodes in channel #1, the electric field along the z axis of LN generates some variation of the refractive index of LN due to the Pockels effect. Accordingly, the resonance wavelength of this channel is shifted, resulting in high-speed wavelength-selective intensity modulation for the channel of λ_1. Similar processes happen in the sequence for the other wavelength channels. After being reflected by the channel of λ_n, the light of all wavelengths has been modulated individually, and the modulated signals finally exit together from the output port.

As shown in Fig. 1(b), the MWG has an effective waveguide width equal to the width W of the straight waveguide in the middle of the cavity region, and the grating period of Λ satisfies the following equation: $n_{\text{eff\_TE0}} + n_{\text{eff\_TE1}} = \lambda_B/\Lambda$, where λ_B is the Bragg wavelength. Linear apodization is applied to the corrugation depth δ in order to realize a high sidelobe suppression ratio for the reflective response. Accordingly, one has $\delta_i = \delta_0(1 - 2|i - N/2|/N)$, where δ_0 is the maximal corrugation depth, N is the total number of the grating period, and $i = 1, \ldots, N$. Figure 2(a) shows the simulated spectral response of the designed MWG at the wavelength band of 1530 to 1580 nm when the TE_0 mode was incident, including the intensity and phase responses of reflection and transmission. Figure 2(b) shows the simulated light propagation in the MWG when operating at 1550 and 1580 nm. It can be seen that the launched TE_0 mode (forward) is reflected and converted to the TE_1 mode (backward) at 1550 nm (around the Bragg wavelength) but transmitted directly at 1580 nm (away from the Bragg wavelength). The mode (de)multiplexer is designed following the method given in our previous work.[51]

For the FP cavity LNOI modulator, the EO modulation bandwidth is mainly limited by the photon lifetime of the cavity.[30] A shorter photon lifetime, corresponding to a lower Q-factor and a larger FWHM bandwidth, is the key to achieve a higher modulation bandwidth, which, however, leads to a lower modulation efficiency as well as a higher optical interchannel cross talk for the DWDM system.[14] As a result, the Q-factor should be chosen optimally. For the present case with a channel-spacing of 200 GHz (1.6 nm) around 1550 nm, the Q-factor of the FP cavity modulator should be >4000 (FWHM bandwidth = 0.38 nm) to make the optical cross talk negligible for signal transmission and should be <5000 to support high-speed transmission of 100 Gbps PAM4 signals. In our design, the absorption loss from the metal electrodes is negligible while the Q-factor is controlled by adjusting the reflectivity of the MWGs.

Deviations from the design often occur in the fabrication, including the etching depth, waveguide width W, period Λ, and corrugation depth δ of MWGs, as well as the random thickness variation of the LN film. The phase response of MWGs and the phase accumulation in the straight section are sensitive to these deviations, making it difficult to align the resonance wavelengths of the fabricated FP cavities as predicted by the theoretical simulation. Meanwhile, the reflectivity of MWGs is also related to the corrugation depth, which in turn affects the Q-factor and extinction ratio (ER) of the resonance in the FP cavity. Although the resonance wavelength depends on

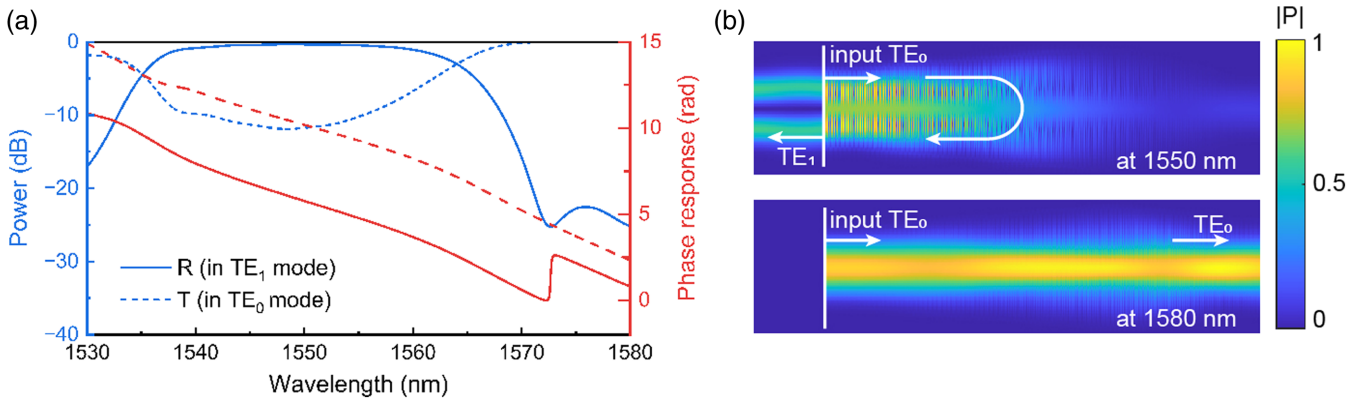

Fig. 2 (a) Simulated intensity (blue) and phase (red) response of the reflected TE_1 mode (solid line) and transmitted TE_0 mode (dotted line) of the MWG with the parameters of $W = 2.6$ μm, $\Lambda = 430$ nm, $\delta_0 = 1.6$ μm, and $N = 110$; (b) simulated light propagation in the designed MWG when operating at 1550 nm (around the Bragg wavelength) and 1580 nm (away from the Bragg wavelength), respectively.

fabrication variations, the channel spacing is predictable. To achieve uniform wavelength spacing as well as efficient modulation for the multichannel FP cavity modulators, the waveguide width W of the straight section in the FP cavities is chosen carefully. Figure 3(a) shows the calculated effective refractive indices n_{eff} of the TE_0 and TE_1 modes in a straight waveguide as the waveguide width W varies, and the inset shows the mode profiles $|\mathbf{E}(x, y)|$. It can be seen that the slope of the mode dispersion curves decreases gradually with the increase of the width W, indicating that the waveguide with a large W is less sensitive to the random fabricated errors in width.

The resonance wavelength variation $|\delta\lambda_{\text{res}}|$ of the FP cavity is also calculated from the spectral responses obtained by the transfer matrix method (TMM) when assuming that the waveguide width is given as $W = W_0 + \delta w$ and the slab thickness is given as $H = H_0 + \delta h$, where $\delta w = \pm 10, \pm 20$ nm and $\delta h = \pm 5$ nm. Here, the waveguide width W_0 is considered to be in the range of 1.7 to 2.9 μm, while the slab thickness H_0 is fixed as 200 nm, as shown in Fig. 3(b). The resonance wavelength variation $|\delta\lambda_{\text{res}}|$ greatly decreases from 0.80 to 0.21 nm for the case with $\delta w = \pm 20$ nm when the waveguide width increases from 1.7 to 2.9 μm. If the width variation can be controlled to be no more than 10 nm, e.g., $\delta w = \pm 10$ nm, the resonance wavelength variation $|\delta\lambda_{\text{res}}|$ greatly decreases to 0.10 nm when the waveguide width increases to 2.9 μm, which is attractive for achieving high uniformity for the wavelengths of the channels. Therefore, it is preferred to choose a broadened waveguide for the FP cavity.

On the other hand, the absorption loss of the metal electrodes might increase when broadening the waveguide. Figure 3(c) shows the calculated metal absorption losses of the TE_0 and TE_1 modes for the cases with $W = 1.7$, 2.0, 2.3, 2.6, and 2.9 μm as the lateral separation S between electrodes varies. As it can be seen, one has to choose a large S to make the metal absorption loss sufficiently low. For example, the lateral separation S should be larger than 5.4, 5.2, 5.3, 5.4, and 5.5 μm for achieving an average absorption loss less than 0.5 dB/cm for the cases with $W = 1.7$, 2.0, 2.3, 2.6, and 2.9 μm, indicating that the modulation efficiency might be lowered with W increasing. In order to evaluate the modulation efficiency, the change of the average effective refractive index Δn_{eff} for unit applied voltage is calculated, as shown in Fig. 3(d). Here, Δn_{eff} is defined as the average of the effective indices of the TE_0 and TE_1 modes. And the electrode separation is set to the allowable minimal value so that the average of the absorption loss of the TE_0 and TE_1 modes is <0.5 dB/cm. Figure 3(d) shows that the modulation efficiency decreases when the waveguide is widened to more than 2.6 μm. The inset in Fig. 3(d) shows the static electric field distribution when an external bias voltage of 10 V is applied. Therefore, we choose the width as $W = 2.6$ μm with the electrode separation of $S = 5.4$ μm by making a trade-off for maximizing the modulation efficiency as well as lowering the

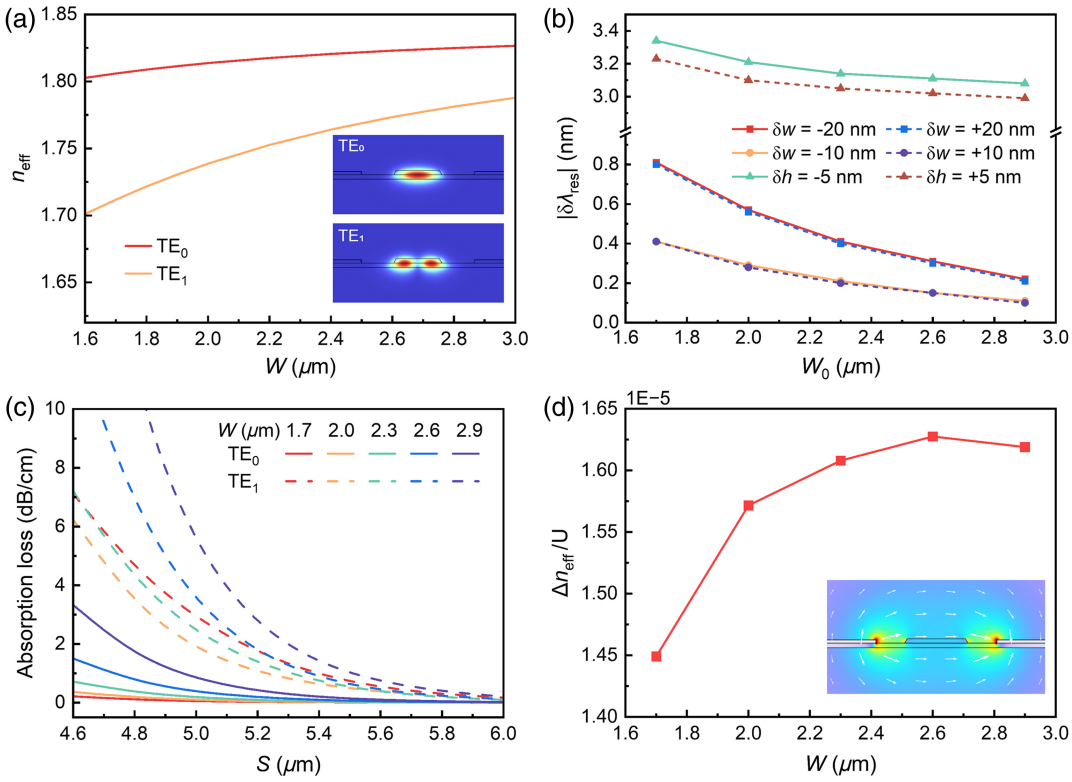

Fig. 3 (a) Calculated effective indices n_{eff} of the TE_0 and TE_1 modes as the waveguide width W varies [inset: mode profiles $|\mathbf{E}(x, y)|$]. (b) Calculated resonance-wavelength variation $|\delta\lambda_{\text{res}}|$ of the FP cavity when assuming that the waveguide width is given as $W = W_0 + \delta w$ and the slab thickness is given as $H = H_0 + \delta h$. (c) Calculated metal absorption loss of the TE_0 and TE_1 modes for $W = 1.7$, 2.0, 2.3, 2.6, and 2.9 μm. (d) Calculated average modulation efficiency $\Delta n_{\text{eff}}/U$ of the TE_0 and TE_1 modes for unit applied voltage when the average absorption loss of the TE_0 and TE_1 modes is 0.5 dB/cm (inset: the static electric field distribution).

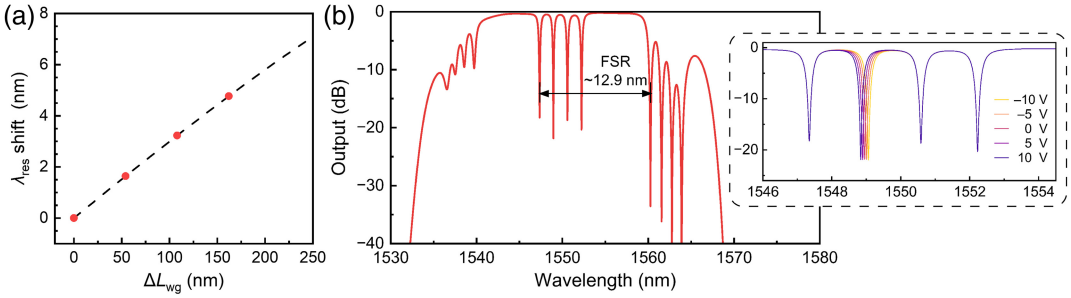

Fig. 4 (a) Calculated resonance wavelength shift with the cavity length variation ΔL_{wg}. (b) Calculated reflective spectrum of the four-channel FP cavity modulators with a channel spacing of 1.6 nm. The inset shows the spectral responses when bias voltages are applied to the second FP cavity (channel #2).

sensitivity of the FP resonance wavelength to the waveguide-width variation.

Finally, the MWG is designed with the following parameters: $W = 2.6\ \mu$m, $\delta_0 = 1.6\ \mu$m, $N = 110$, and $\Lambda = 430$ nm. In simulation, the MWG exhibits a reflectivity of 0.9 and a 1-dB Bragg bandwidth of ~20 nm centered around 1550 nm, ensuring that all FP cavities resonating in the flat-top passband of MWGs have similar performance in Q-factors and ERs. For the mode (de)multiplexer, the core widths at the input/output ends of waveguides A and B are chosen as $(w_{a1}, w_{a2}) = (1, 2.6)\ \mu$m, $(w_{b1}, w_{b2}) = (0.5, 0.2)\ \mu$m, while the taper lengths $(L_{01}, L_{12}, L_{23}) = (70, 100, 30)\ \mu$m and the gap widths $(w_{g1}, w_{g2}, w_{g3}) = (2.2, 0.25, 1.2)\ \mu$m. The straight section between two MWGs of the first channel has a length of $L_{wg} = 6\ \mu$m. Figure 4 shows the calculated results of the four-channel FP cavity modulators by using TMM. From Fig. 4(a), one has a resonance wavelength shift of 0, 1.6, 3.2, and 4.8 nm by introducing some length variation ΔL_{wg} of 0, 54, 108, and 162 nm for the straight section in the FP cavity, which meets the requirement for achieving a channel spacing of 1.6 nm (corresponding to 200 GHz) in DWDM systems. Figure 4(b) shows the calculated reflective spectrum of the four-channel FP cavity modulators in cascade. It can be seen that there are four resonant notches with a channel spacing of 1.6 nm, as expected, and the FSR is around 12.9 nm (which is sufficiently large to cover all four channels). The inset in Fig. 4(b) shows the spectral responses when the second FP cavity (channel #2) is modulated by applying a bias voltage of −10, −5, 0, 5, and 10 V, respectively. In this case, the modulation efficiency is given by 11.2 pm/V.

3 Fabrication and Characterization

The chip was fabricated with a commercial x-cut LNOI wafer, and the nominal thickness of the LN layer is 400 nm. The device structure was first patterned by an electron-beam lithography process after spin-coating MaN2403 resist, and the LN layer was then etched 200 nm by Ar^+ plasma. The electrodes were formed with a lift-off process, and the thicknesses of the titanium and gold electrodes are 10 and 150 nm, respectively. Figure 5(a) shows the optical microscope image of the fabricated chip for DWDM transmitters, showing a compact footprint of only ~0.78 mm × 0.58 mm. Figure 5(b) shows the scanning electron microscope (SEM) images of the FP cavities, while the zoomed-in views for the MWG and the mode (de)multiplexer are, respectively, shown in Figs. 5(c) and 5(d).

The fabricated four-channel LNOI photonic chip was first characterized repeatedly by using the setup consisting of a broadband amplified spontaneous emission light source and an optical spectrum analyzer. Figure 6(a) shows the spectral response at the output port when operating under a fixed temperature of 25°C, normalized with the transmission of a pair of grating couplers when there is no external electrical field applied. The fabricated FP cavities have an overall EL as low as 1.3 dB and ERs over 20 dB, with measured Q-factors about 4500. A set of resonances is in the range of 1545 to 1551 nm, with the FSR around 13.1 nm. It can be seen that there is a discrepancy of the resonance wavelengths between the measurement results and the simulation one in Fig. 4(b), which is presumably due to some deviation of the etch depth from the design value of 200 nm. Although the measured spectrum is not exactly consistent with the simulation ones, the channel spacing of ~1.6 nm was obtained as expected and the fluctuations are as small as only ~0.12 nm. The wavelengths for these four channels can be perfectly aligned with the DWDM grids by controlling the temperature and introducing some static electrical field, as shown in Fig. 6(b). For example, here we set the temperature as 14°C for achieving some blueshift and then introduce different bias voltages of $U = -10$, 4.5, −6, and −2 V for these four modulators for perfectly aligning the four channels to the wavelengths of 1545.32, 1546.92, 1548.52, and 1550.12 nm as desired, respectively. In this case, the channel spacing of 1.6 nm (200 GHz) is achieved perfectly. Figure 6(c) shows the measured resonance wavelength shift, which increases linearly as the applied voltage varies from −20 to 20 V, indicating a modulation efficiency of ~9 pm/V, which is slightly lower than the calculation one in Fig. 4(b) because the separation S of the electrodes is slightly increased compared to the design value.

The high-frequency small-signal EO responses were then characterized using the experiment setup composed of a tunable continuous-wave (CW) laser (Keysight 81940A) and a lightwave component analyzer (LCA, Ceyear 6433L), as shown in Fig. 6(d). The measurements of four channels were performed one by one in sequence, limited by the channel number of the radio-frequency (RF) source. For the channel #i with the resonance wavelength $\lambda_{res,i}$, the wavelength of the laser source was tuned with a wavelength detuning of $\lambda_i - \lambda_{res,i} = 0.15$ nm; the corresponding insertion loss is ~6.5 dB. After being rotated to TE polarization by a three-paddle polarization controller, light was coupled into and out of the chip through grating couplers using single-mode fibers. The small RF signal generated by

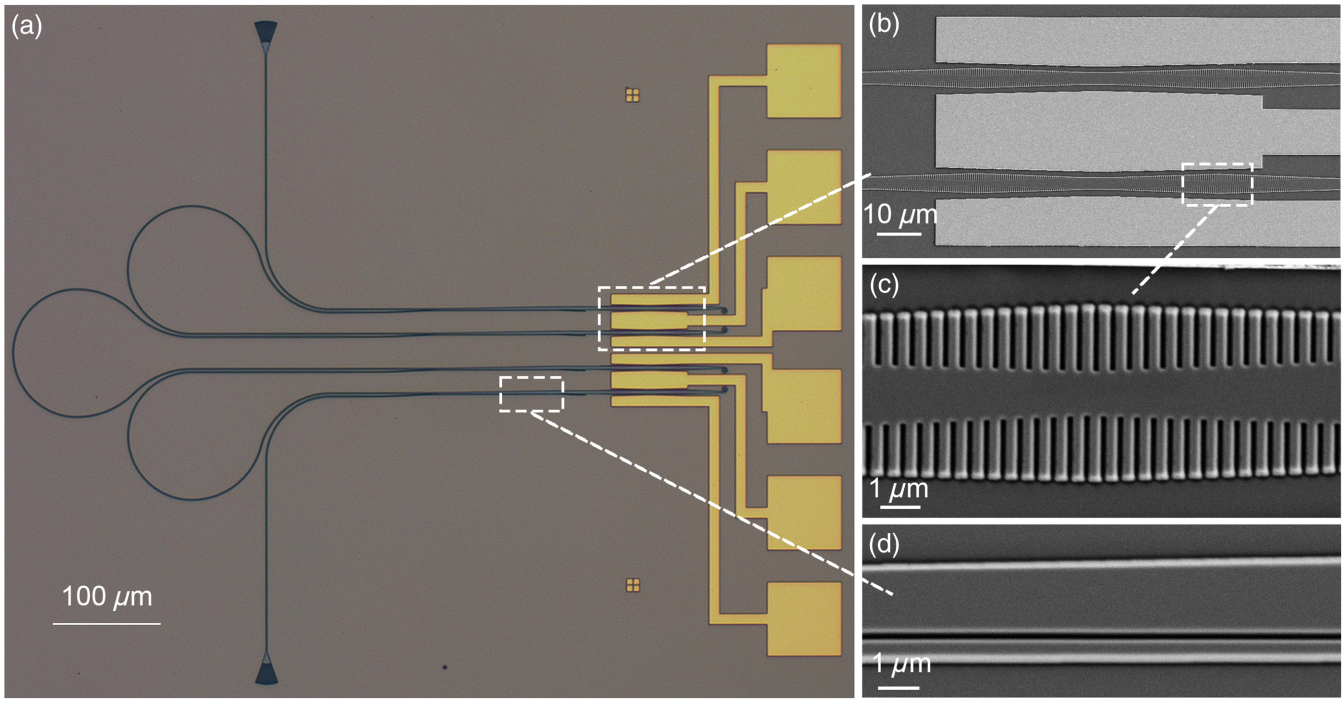

Fig. 5 (a) Microscope image of the fabricated four-channel chip for DWDM transmitters; SEM images of (b) the FP cavities, (c) the MWG, and (d) the mode (de)multiplexer.

the microwave module of the LCA was applied to electrodes in channel #*i* via a GS RF probe (GGB, DC to 67 GHz). Finally, the modulated light signal was collected by a high-speed photodetector in the LCA optical module and finally received by the microwave module. Since the LNOI FP cavities have the temperature sensitivity of 32 pm/°C for the resonance wavelengths, the thermal controller was introduced to set the working temperature at 25°C, in which case the EO responses were highly stable. Figure 6(e) shows the measured small-signal EO responses S_{21} for all the four channels, normalized with the value at 0.1 GHz, respectively. It can be seen the measured EO 3-dB bandwidths are higher than 67 GHz (which is beyond the VNA limit). Enlarging the wavelength detuning can further expand the EO 3-dB bandwidth due to the peak enhancement,[30] at the expense of modulation efficiency suppression at low-frequency range.

The interchannel EO cross talk in the current configuration is composed of two aspects. First, since light at all wavelengths passes through the same waveguide and is coupled into the FP cavities of all channels, the spectral isolation between adjacent channels might be limited. For example, the incident light with the wavelength for channel #2 might also be modulated gently by the FP cavity modulators of the adjacent channels (i.e., #1 and #3). The FWHM bandwidth of the cavities' responses has been designed to be sufficiently small to suppress the optical cross talk. Second, there is some electrical cross talk from adjacent channels if the separation is not far enough, indicating that the round-trip optical path of the FP cavity for channel #*i* might be modulated by RF signals applied to the other channels. In the experiment characterizing interchannel EO cross talk to channel #1 (or channel #2), the setup was the same as that of the small-signal EO response measurement. The input light was kept with a wavelength detuning $\lambda - \lambda_{\mathrm{res},1}$ (or $\lambda - \lambda_{\mathrm{res},2}$) as 0.15 nm, while the RF signal from LCA was applied to electrodes of the other three channels, one by one. The output optical signals were then collected by the LCA. Particularly, the measured results were normalized with the small-signal EO response of channel #1 or #2, respectively.[52] Figure 6(e) shows the interchannel EO cross talk of modulators from other channels to channel #1 and channel #2. As shown in Fig. 6(f), the cross talk mainly occurs between channel #1 and channel #2, which share the same ground electrode. For channel #2, in addition, the cross talk also comes from channel #3 at a high frequency above 50 GHz whose signal electrodes are very close. Due to the symmetrical arrangement, the EO cross talk to channel #3 and channel #4 should be consistent with that of channel #2 or channel #1. As shown in Fig. 6(e), the total interchannel EO cross talk is less than –7 dB in the frequency range of 0.01 to 67 GHz.

Finally, high-speed data transmissions were characterized experimentally for all channels in sequence. Here, a pseudo-random binary sequences signal with a length of $2^7 - 1$ was generated by an arbitrary waveform generator connected with a clock source. The driver signal was fed to a linear RF amplifier (SHF S807C) followed by a 6-dB attenuator to avoid reflection damage before being coupled to the electrodes via the probe, which was applied to the modulator with a peak-to-peak voltage V_{pp} of 1.8 V. A tunable CW laser source with 13 dBm output power near the resonance wavelength was fed into the input port, while the optical power entering the chip was 8.5 dBm regarding the coupling loss of 4.5 dB. In this case, no nonlinear effects or optical damage was observed. If the optical power significantly increases to hundreds of dBm for some specific applications, nonlinear effects or optical damage might happen.[53] The modulated signals were amplified by an erbium-doped fiber amplifier with an optical bandpass filter and then collected by an

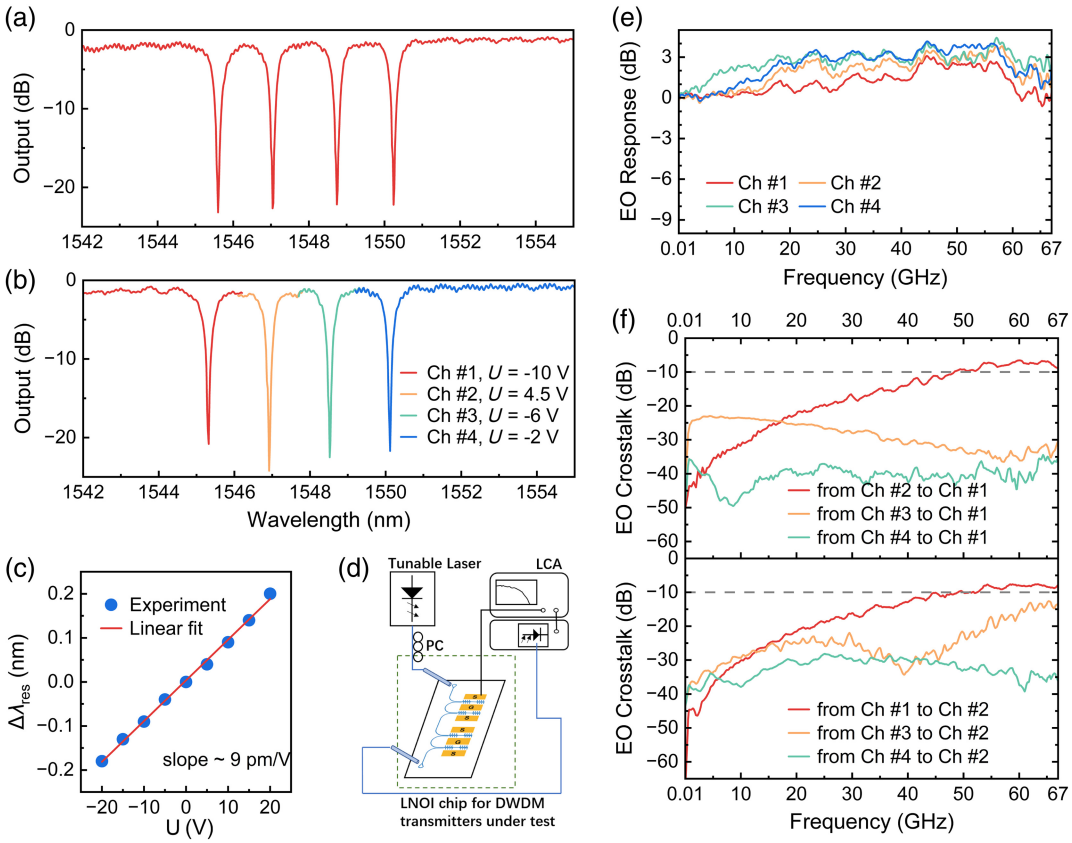

Fig. 6 (a) Original spectral response of the fabricated four-channel chip for DWDM transmitters. (b) Calibrated spectral responses with the channel wavelengths aligned to the DWDM grids by controlling the temperature and introducing static electric field individually. (c) Measured resonance wavelength shifts as the applied voltage varies from –20 to 20 V. (d) Experiment setup for measurement of small-signal EO responses and interchannel EO cross talk. Measured EO responses S_{21} for all the four channels (e) and interchannel RF cross talk of modulators (f).

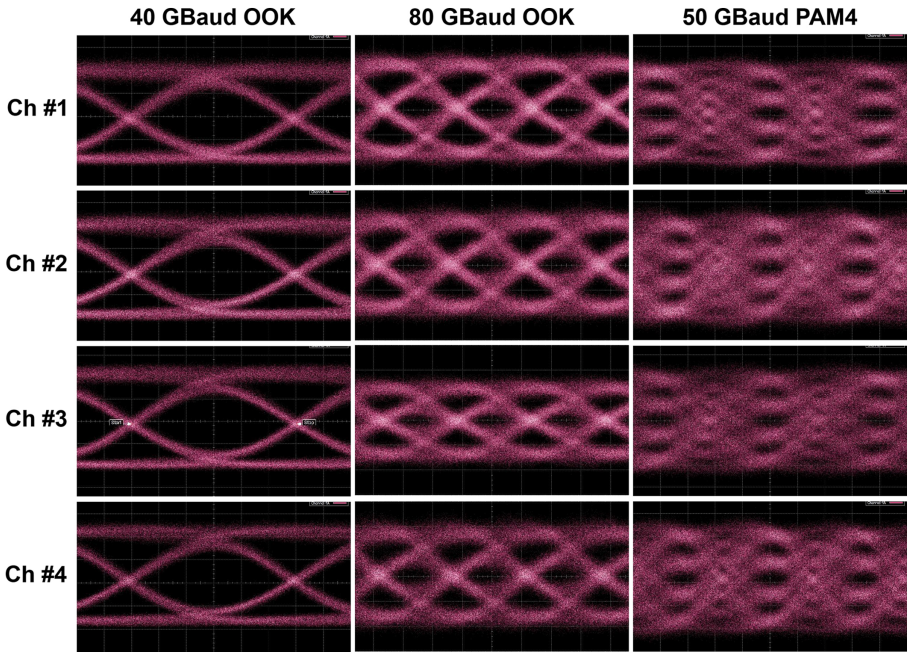

Fig. 7 Measured eye diagrams for the four channels where the modulated electrical signals were generated individually and applied to each modulator one by one.

electrical sampling oscilloscope (Keysight 86100D). Figure 7 shows the measured eye diagrams for the four channels with the modulated 40/80 Gbps OOK signals as well as the modulated 100 Gbps (50 GBaud) PAM4 signals. For the 40 Gbps OOK signals, the wavelength detuning was set as 0.10 nm to realize high ERs of ~4.5 dB and a signal-to-noise ratio (SNR) of >5.8 dB for all four channels. When the data rate increases to 80 and 100 Gbps, a wavelength detuning of 0.18 nm was introduced for an improved EO bandwidth, causing the ERs and SNRs of 80 Gbps OOK signals to drop to 0.8 and 2.5 dB, respectively. High-order modulation schemes such as PAM8 are also possible for the current device, in principle. However, due to the insufficient EO coefficient of LN and limited linear region of the Lorentzian shape, a sufficiently high V_{pp} with the assistance of DSP is required to generate high-quality signals. For the present LNOI photonic chip for DWDM transmitters, the total data transmission rate is up to 400 Gbps when modulated with 50 GBaud PAM4 signals. For each FP cavity modulator, the capacitance is about 6.3 fF, and the corresponding energy consumption for modulation is estimated to be only ~5.1 fJ/bit for the 80 Gbps OOK signals when operating with the V_{pp} of 1.8 V, according to the formula of $C V_{pp}^2/4$ given in Ref. 54. Since only FP cavity modulators are integrated on the chip, other energy consumption for the laser, RF driver, and thermal management is not included here. With the number of channels increasing, the total power consumption could be significant.

Limited by the experimental setup, the signals for the four channels were generated individually by applying the external RF voltage one by one. In order to evaluate the impact of the interchannel EO cross talk on the signals, a numerical simulation was conducted according to the experimental data in Figs. 6(e) and 6(f). The input pseudo-random signals pass through a system with the frequency response according to Fig. 6(d), and are output as the generated signals with no interchannel RF cross talk. Then cross talks from the other three channels are superimposed on the signals according to the frequency response in Fig. 6(f) with arbitrary time delays.[55] Low-pass filtering ($f_{3\,dB} = 67$ GHz) and white noise are then introduced to be similar to the real case. Figures 8(a) and 8(b) present the simulated eye diagrams without and with RF cross talks from other channels, respectively, for the cases with 80 GBaud OOK and 50 GBaud PAM4 signals. It shows that signals are indeed affected by the interchannel cross talk and are still legible, indicating that the present LNOI photonic chip for DWDM transmitters potentially supports 80 GBaud OOK and 50 GBaud PAM4 data transmission in real applications.

4 Discussion and Conclusion

In the present demonstration of LNOI photonic chips for DWDM transmitters with narrow channel spacings, one of the big challenges is to achieve uniform channel spacing for all channels, even when some inevitable fabrication variations exist. As given by the detailed analysis in Sec. 2, the waveguide width for the straight section of the FP cavity is chosen carefully to achieve an improved fabrication tolerance. However, as shown in Fig. 3(b), the random deviation of the LN slab thickness should be considered because it influences the resonance wavelength more than the width deviation. In our experiments, the etching depth is quite uniform according to the characterization of the etching process. However, the commercially available 3- or 4-in. LNOI wafers typically have a deviation of $\pm \sim 5$ nm for the thickness of the LN thin film. To discuss the uniformity, Fig. 9 shows the standard deviation σ of

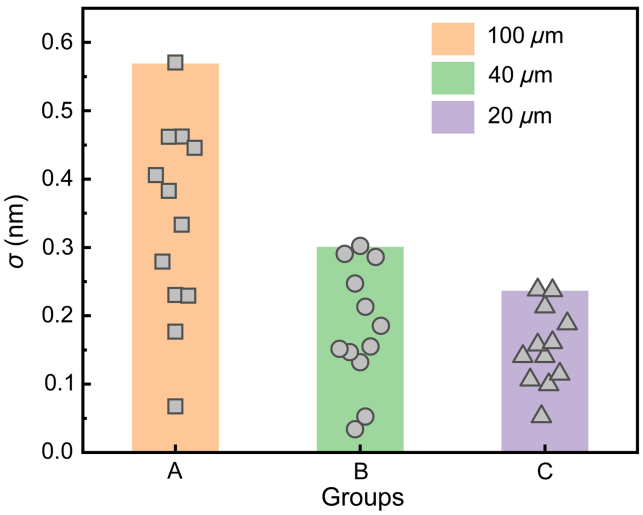

Fig. 9 Measured standard deviation σ of channel spacings of three groups of FP cavity modulators. In groups A, B, and C, modulators are placed with a separation of 100, 40, and 20 μm between the adjacent two, respectively.

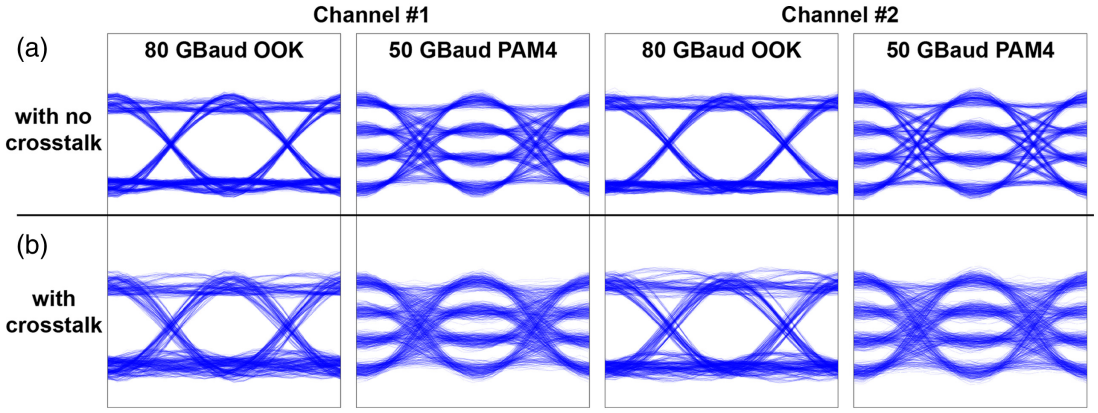

Fig. 8 Numerically calculated eye diagrams for channel #1 and channel #2 (a) without cross talk and (b) with cross talk from other channels, corresponding to the measured results in Fig. 6(e).

measured channel spacings of three groups of devices fabricated on the same chip, where a dot is for a device. Each device consists of four channels of FP cavity modulators, which are placed with a separation of 100, 40, and 20 μm between the adjacent two in groups A, B, and C, respectively. There are 12 devices in each group to ensure the reliability of statistics conclusions. Here, the standard deviation is given by $\sigma = \sqrt{\sum_{i=1}^{3}(\Delta\lambda_{\mathrm{ch}\_i} - \mu)^2/3}$, where $\Delta\lambda_{\mathrm{ch}\_i}$ is the channel spacing for the four-channel device ($i = 1, 2, 3$), and μ is the average of the channel spacings $\Delta\lambda_{\mathrm{ch}\_i}$. It can be seen that the standard deviation σ decreases greatly when the FP cavity modulators are placed closely with a reduced separation as small as 20 μm, indicating that the present design with ultracompact footprints provides a new option for DWDM transmitters, which not only enhances the integration density of the chip but also improves the uniformity of the components in an array. Note that the present chip can be extended to have more channels (e.g., $N_{\mathrm{ch}} = 8$) when needed if the FSR of the FP cavity is as large as 13.1 nm. The FSR can be improved further by reducing the FP cavity length and increasing the reflection bandwidth of MWGs. Meanwhile, the challenges in channel spacing uniformity and wavelength stabilization as well as thermal management will become prominent, which are the common issue for large-scale transmitters.[56]

In conclusion, we have proposed a compact LNOI photonic chip for DWDM transmitters, for the first time to our knowledge, by using 2×2 FP cavity EO modulators in cascade. The fabricated photonic chip features four wavelength channels with a narrow channel spacing of ~1.6 nm, which is the smallest one reported for LNOI optical transmitters. The photonic chip with four channels shows a footprint as compact as 0.78 mm × 0.58 mm and a low EL of ~1.3 dB. For these FP cavities, the separations between them have been minimized to 20 μm, and the LNOI photonic waveguides in the cavity sections have been broadened to 2.6 μm. In this way, the resonance wavelengths of these FP cavities become insensitive to the core-width variation and have been aligned precisely with a channel spacing of ~1.6 nm. According to the measured small-signal EO responses, one sees that the fabricated FP cavity modulators have interchannel EO cross talk of less than −7 dB in the range of 0.01 to 67 GHz while they work very well with a 3-dB bandwidth of >67 GHz. Finally, we have demonstrated high-speed data transmissions with 4×80 Gbps OOK signals and 4×100 Gbps PAM4 signals for four channels, enabling a total data transmission rate of up to 400 Gbps. With the thermal control, the chip performs stably during our long-term measurement owing to the high stability of LN,[57] which shows the potential of being used practically for our LNOI photonic chip. All these performance metrics indicate our LNOI photonic chip is still very promising for next-generation high-capacity optical communication systems.

Disclosures

The authors declare no conflicts of interest.

Code and Data Availability

The data that support the plots within this paper and other findings of this study are available from the corresponding author upon reasonable request.

Acknowledgments

This work was supported by the National Key Research and Development Program of China (Grant Nos. 2018YFB2200200 and 2018YFB2200201), the National Natural Science Foundation of China (NSFC) (Grant Nos. 92150302, 62135012, U23B2047, and 62321166651), the Zhejiang Provincial Natural Science Foundation (Grant No. LDT23F04012F05), the Zhejiang Provincial Key Research and Development Program (Grant No. 2021C01199), and the Leading Innovative and Entrepreneur Team Introduction Program of Zhejiang (Grant No. 2021R01001).

References

1. A. H. Gnauck et al., "High-capacity optical transmission systems," *J. Light. Technol.* **26**, 1032–1045 (2008).
2. Y. Shi et al., "Silicon photonics for high-capacity data communications," *Photonics Res.* **10**, A106–A134 (2022).
3. Y. Su et al., "Scalability of large-scale photonic integrated circuits," *ACS Photonics* **10**, 2020–2030 (2023).
4. Y. Huang et al., "High-bandwidth Si/In_2O_3 hybrid plasmonic waveguide modulator," *APL Photonics* **7**, 051301 (2022).
5. H. Ishio, J. Minowa, and K. Nosu, "Review and status of wavelength-division-multiplexing technology and its application," *J. Light. Technol.* **2**, 448–463 (1984).
6. D. Dai and J. E. Bowers, "Silicon-based on-chip multiplexing technologies and devices for peta-bit optical interconnects," *Nanophotonics* **3**, 283–311 (2014).
7. Y. Suzaki et al., "Monolithically integrated eight-channel WDM modulator with narrow channel spacing and high throughput," *IEEE J. Sel. Top. Quantum Electron.* **11**, 43–49 (2005).
8. S. Cheung et al., "Demonstration of a 17 × 25 Gb/s heterogeneous III-V/Si DWDM transmitter based on (de-)interleaved quantum dot optical frequency combs," *J. Light. Technol.* **40**, 6435–6443 (2022).
9. R. Nagarajan et al., "Large-scale photonic integrated circuits," *IEEE J. Sel. Top. Quantum Electron.* **11**, 50–65 (2005).
10. M. Moralis-Pegios et al., "4-channel 200 Gb/s WDM O-band silicon photonic transceiver sub-assembly," *Opt. Express* **28**, 5706–5714 (2020).
11. C. Li et al., "Hybrid WDM-MDM transmitter with an integrated Si modulator array and a micro-resonator comb source," *Opt. Express* **29**, 39847–39858 (2021).
12. Y. Yuan et al., "A 5 × 200 Gbps microring modulator silicon chip empowered by two-segment Z-shape junctions," *Nat. Commun.* **15**, 918 (2024).
13. C. Sun et al., "A 45 nm CMOS-SOI monolithic photonics platform with bit-statistics-based resonant microring thermal tuning," *IEEE J. Solid-State Circuits* **51**, 893–907 (2016).
14. J. Sharma et al., "Silicon photonic microring-based 4 × 112 Gb/s WDM transmitter with photocurrent-based thermal control in 28-nm CMOS," *IEEE J. Solid-State Circuits* **57**, 1187–1198 (2022).
15. P.-H. Chang et al., "A 3D integrated energy-efficient transceiver realized by direct bond interconnect of co-designed 12 nm FinFET and silicon photonic integrated circuits," *J. Light. Technol.* **41**, 6741–6755 (2023).
16. Y. Wang et al., "Silicon photonics chip I/O for ultra high-bandwidth and energy-efficient die-to-die connectivity," in *2024 IEEE Custom Integrated Circuits Conf. (CICC)*, IEEE, pp. 1–8 (2024).
17. E. Andrianopoulos et al., "Integrated 800 Gb/s O-band WDM optical transceiver enabled by hybrid InP-polymer photonic integration," *J. Opt. Commun. Network* **16**, D44–D52 (2024).
18. M. Levy et al., "Fabrication of single-crystal lithium niobate films by crystal ion slicing," *Appl. Phys. Lett.* **73**, 2293–2295 (1998).

19. A. Boes et al., "Status and potential of lithium niobate on insulator (LNOI) for photonic integrated circuits," *Laser Photon. Rev.* **12**, 1700256 (2018).
20. D. Zhu et al., "Integrated photonics on thin-film lithium niobate," *Adv. Opt. Photonics* **13**, 242–352 (2021).
21. M. Zhang et al., "Integrated lithium niobate electro-optic modulators: when performance meets scalability," *Optica* **8**, 652–657 (2021)
22. B. Pan et al., "Perspective on lithium-niobate-on-insulator photonics utilizing the electro-optic and acousto-optic effects," *ACS Photonics* **10**, 2078–2090 (2023).
23. B. Pan et al., "Demonstration of high-speed thin-film lithium-niobate-on-insulator optical modulators at the 2-μm wavelength," *Opt. Express* **29**, 17710–17717 (2021).
24. C. Wang et al., "Integrated lithium niobate electro-optic modulators operating at CMOS-compatible voltages," *Nature* **562**, 101–104 (2018).
25. P. Kharel et al., "Breaking voltage–bandwidth limits in integrated lithium niobate modulators using micro-structured electrodes," *Optica* **8**, 357–363 (2021).
26. G. Chen et al., "High performance thin-film lithium niobate modulator on a silicon substrate using periodic capacitively loaded traveling-wave electrode," *APL Photonics* **7**, 026103 (2022).
27. C. Wang et al., "Nanophotonic lithium niobate electro-optic modulators," *Opt. Express* **26**, 1547–1555 (2018).
28. M. Li et al., "Lithium niobate photonic-crystal electro-optic modulator," *Nat. Commun.* **11**, 4123 (2020).
29. B. Pan et al., "Compact electro-optic modulator on lithium niobate," *Photonics Res.* **10**, 697–702 (2022).
30. B. Pan et al., "Ultra-compact lithium niobate microcavity electro-optic modulator beyond 110 GHz," *Chip* **1**, 100029 (2022).
31. Y. Xue et al., "Breaking the bandwidth limit of a high-quality-factor ring modulator based on thin-film lithium niobate," *Optica* **9**, 1131–1137 (2022).
32. K. Chen et al., "Four-channel CWDM transmitter chip based on thin-film lithium niobate platform," *J. Semicond.* **43**, 112301 (2022).
33. H. Liu et al., "Ultra-compact lithium niobate photonic chip for high-capacity and energy-efficient wavelength-division-multiplexing transmitters," *Light Adv. Manuf.* **4**, 133–142 (2023).
34. Q. Fang et al., "WDM multi-channel silicon photonic receiver with 320 Gbps data transmission capability," *Opt. Express* **18**, 5106–5113 (2010).
35. S. Cheung et al., "Ultra-compact silicon photonic 512 × 512 25 GHz arrayed waveguide grating router," *IEEE J. Sel. Top. Quantum Electron.* **20**, 310–316 (2014).
36. D. Dai et al., "Monolithically integrated 64-channel silicon hybrid demultiplexer enabling simultaneous wavelength- and mode-division-multiplexing," *Laser Photon. Rev.* **9**, 339–344 (2015).
37. A. M. Prabhu et al., "Extreme miniaturization of silicon add–drop microring filters for VLSI photonics applications," *IEEE Photonics J.* **2**, 436–444 (2010).
38. T. Dai et al., "Bandwidth and wavelength tunable optical passband filter based on silicon multiple microring resonators," *Opt. Lett.* **41**, 4807 (2016).
39. D. Liu et al., "High-order adiabatic elliptical-microring filter with an ultra-large free-spectral-range," *J. Light. Technol.* **39**, 5910–5916 (2021).
40. S. Robinson and R. Nakkeeran, "Photonic crystal ring resonator-based add drop filters: a review," *Opt. Eng.* **52**, 060901 (2013).
41. Z. Wang et al., "On-chip arrayed waveguide grating fabricated on thin film lithium niobate," arXiv2305.18059 (2023).
42. Y. Yu et al., "Wavelength-division multiplexing on an etchless lithium niobate integrated platform," *ACS Photonics* **9**, 3253–3259 (2022).
43. A. Pan et al., "Fundamental mode hybridization in a thin film lithium niobate ridge waveguide," *Opt. Express* **27**, 35659–35669 (2019).
44. B. Pan et al., "Compact racetrack resonator on $LiNbO_3$," *J. Light. Technol.* **39**, 1770–1776 (2021).
45. K. Luke et al., "Wafer-scale low-loss lithium niobate photonic integrated circuits," *Opt. Express* **28**, 24452–24458 (2020).
46. P. Dong et al., "Reconfigurable add-drop filter based on an anti-symmetric multimode photonic crystal nanobeam cavity in a silicon waveguide," *Opt. Express* **30**, 17332–17339 (2022).
47. A. Dideban, H. Habibiyan, and H. Ghafoorifard, "Photonic crystal channel drop filter based on ring-shaped defects for DWDM systems," *Phys. E Low-Dimensional Syst. Nanostructures* **87**, 77–83 (2017).
48. C. Sun et al., "A 45 nm CMOS-SOI monolithic photonics platform with bit-statistics-based resonant microring thermal tuning," *IEEE J. Solid-State Circuits* **51**, 893–907 (2016).
49. W. Zhao et al., "96-Channel on-chip reconfigurable optical add-drop multiplexer for multidimensional multiplexing systems," *Nanophotonics* **11**, 4299–4313 (2022).
50. C. Zhang et al., "Silicon photonic wavelength-selective switch based on an array of adiabatic elliptical-microrings," *J. Light. Technol.* **41**, 5660–5667 (2023).
51. D. Dai et al., "10-channel mode (de)multiplexer with dual polarizations," *Laser Photon. Rev.* **12**, 1700109 (2018).
52. L. Jiang et al., "Electro-optic crosstalk in parallel silicon photonic Mach-Zehnder modulators," *J. Light. Technol.* **36**, 1713–1720 (2018).
53. S. Liu, Y. Zheng, and X. Chen, "Cascading second-order nonlinear processes in a lithium niobate-on-insulator microdisk," *Opt. Lett.* **42**, 3626–3629 (2017).
54. D. A. B. Miller, "Energy consumption in optical modulators for interconnects," *Opt. Express* **20**, A293–A308 (2012).
55. Z. Yu et al., "High-dimensional communication on etchless lithium niobate platform with photonic bound states in the continuum," *Nat. Commun.* **11**, 2602 (2020).
56. T. Kobayashi et al., "Coherent optical transceivers scaling and integration challenges," *Proc. IEEE* **110**, 1679–1698 (2022).
57. E. Obrzud et al., "Stability of lithium niobate integrated photonics in nonlinear and metrology applications," in *Conf. Lasers Electro-Optics, Optica Publishing Group*, p. JW1A.167 (2021).

Hongxuan Liu is a doctoral candidate student at the College of Optical Science and Engineering, Zhejiang University, Hangzhou, China. She received her BE degree in optoelectronic information science and engineering from Huazhong University of Science and Technology, Wuhan, China. Her current research focuses on the study of integrated optics for electro-optic modulator.

Bingcheng Pan received his PhD from the College of Optical Science and Engineering, Zhejiang University in 2023. He received his BS degree from Huazhong University of Science and Technology. His current research interests include electro- and acousto-optics on lithium niobate.

Huan Li received his BE degree in electrical engineering from Tsinghua University and his PhD in electronic engineering from the University of Minnesota Twin Cities. Later, he was a postdoctoral scholar at the University of Minnesota Twin Cities and University of Washington. He is currently a professor in the College of Optical Science and Engineering at Zhejiang University (ZJU). His research interests include nano optomechanical systems, integrated acoustic-optics, and large-scale photonic computing/switch networks.

Zejie Yu obtained his bachelor's degree in optical engineering from ZJU and his PhD in electronic engineering from Chinese University of Hong Kong. Later, he was a postdoctoral fellow in the same department. In September 2020, he joined the College of Optical Science and Engineering of Zhejiang University as a ZJU100 Young professor. He mainly works in the area of silicon-based integrated photonic devices and chips, seeking applications in optical communication, computation, and sensing.

Liu Liu received his BEng degree in information engineering from Zhejiang University, China, in 2002, and his PhD in photonics from the Royal Institute of Technology, Sweden, in 2006. He joined South China Normal University in 2011 and Zhejiang University in 2019. Currently, he is a professor in the College of Optical Science and Engineering at Zhejiang University. His current research area is heterogeneous integration and silicon nanophotonic devices.

Yaocheng Shi received his BEng degree from the Department of Optical Engineering, Zhejiang University, Hangzhou, China, in 2003, and his PhD from Royal Institute of Technology (KTH), Stockholm, Sweden, in 2008. Then, he joined Zhejiang University as an assistant professor and became a professor in December 2016. He has authored more than 100 refereed international journal papers. His research activities are in the photonic integrated devices.

Daoxin Dai received his BEng degree from ZJU, and his PhD from Royal Institute of Technology, Sweden, in 2000 and 2005, respectively. Currently, he is the Qiushi Distinguished Professor of ZJU. He is leading the silicon integrated nanophotonics group at ZJU. His group is working on silicon integrated nanophotonic devices/circuits for optical communications, optical interconnections, as well as optical sensing.